J Eng Math (2011) 71:109–130
DOI 10.1007/s10665-010-9447-z

Two-fluid pressure-driven channel flow with wall deposition and ageing effects

D. Sileri · K. C. Sahu · O. K. Matar

Received: 1 April 2010 / Accepted: 8 December 2010 / Published online: 27 January 2011
© Springer Science+Business Media B.V. 2011

Abstract Two-fluid, stratified pressure-driven channel flow is studied in the limit of small viscosity ratios. Cases are considered in which the core fluid undergoes phase separation that results in the 'precipitation' of a distinct phase and the formation of a wall layer; these situations are common in the oil industry where 'fouling' deposits are formed during the flow. The thickness of this layer increases as a result of continual deposition through Stefan-like fluxes, which are related to the phase behaviour of the core fluid through a chemical equilibria model that treats the fluid as a bi-component mixture. The deposit also undergoes an 'ageing' process whereby its viscosity increases due to the build-up of internal structure; the latter is modelled here via a Coussot-type relation. Lubrication theory is used in the wall layer and an integral balance in the core fluid wherein inertial effects are important. By choosing appropriate semi-parabolic velocity and temperatures closures for the laminar flow in the channel core, and a closure relation for the wall layer rheology, evolution equations are derived that describe the flow dynamics. In the presence of ageing but absence of deposition, it is demonstrated how the time-varying deposit rheology alters the wave dynamics; for certain parameter ranges, these effects can give rise to the formation of steep waves and what appears to be finite-time 'blow-up'. With both ageing and deposition, the spatio-temporal evolution of the deposit is shown together with the increase in the deposition rate with increasing temperature difference between the wall and the inlet.

Keywords Complex rheology · Fouling · Nonlinear waves · Thin films

1 Introduction

The dynamics of thin films has attracted a great deal of attention in the literature due to its importance in many industrial applications. These applications range from coating-flow technology [1], chemical-engineering unit operations such as distillation, condensers and heat exchangers, as well as microfluidics [2,3]. Thin-film flows also have

D. Sileri · O. K. Matar (✉)
Department of Chemical Engineering, Imperial College, London SW7 2AZ, UK
e-mail: o.matar@imperial.ac.uk

K. C. Sahu
Department of Chemical Engineering, Indian Institute of Technology Hyderabad, Ordnance Factory Estate, Yeddumailaram 502205, Andhra Pradesh, India

applications in biophysical and biomedical settings such as pulmonary flows, involving the delivery of surfactant to the lung airways [4,5], tear-film rupture [6], and bio-adhesion [7].

There has been a large number of studies involving thin films over the last three decades, which have focussed on a variety of effects. These include intermolecular forces, capillarity, thermocapillarity, gravity, centrifugation, and electrostatics, and have accounted for the presence of chemical additives, evaporation and condensation, flow over structured, flexible, and porous media, with moving contact lines. Methods ranging from asymptotic techniques to full-scale numerical simulations, and small- and large-scale experiments have been employed in investigating thin films and elucidating a variety of phenomena and instabilities which include wave-formation, dewetting, rupture, and fingering. Thin-film research has also been covered by a number of major reviews [8–10] which highlight the important contributions to this area. Yet, in spite of the large amount of research conducted on thin films, problems involving two-fluid thin-film flows with phase changes leading to deposition and complex, time-varying rheology have not received much attention; this is the subject of the present paper.

We consider the case of pressure-driven flow in a horizontal, rectangular channel where a fluid undergoes phase separation as a result of temperature variations, which results in the formation of a wall layer. Such problems arise in applications involving the deposition of asphaltenic phases on the walls of heat-exchanger units in crude-oil distillation refineries [11,12]. This is a rather complex process, which depends on the fluids being processed, the operating conditions, the heat-exchanger metallurgies and their configurations. The fluids, which correspond to mixtures of crude oils, comprise many hundreds of constituents that include base hydrocarbons (aliphatics, aromatics, resins, asphaltenes, etc.), hetero-atoms, metals, aqueous components, particulates and dissolved gases. All these factors influence the chemistry, physics, thermodynamics and hydrodynamics of fluid-surface interactions under aggressive operating conditions. In the early stages of crude-oil fouling, a 'gel-like' layer is first formed on the wall surface which then undergoes sharp changes in its rheology due to thermal, chemical and physico-chemical factors, causing it to harden, complicating its removal. The interaction between this layer and a fast-flowing layer of lower viscosity overlying it, in the presence of the afore-mentioned complexities, will be studied here.

The deposited wall layer is treated as a distinct phase whose thickness increases through continual deposition. This phase also undergoes a process of 'ageing', which may be due to a 'jamming' transition [13,14] of the particulate phase confined within the deposit leading to structure-building in the deposit, referred to in this paper as 'structuration' [14]; this structure must be broken in order for the material to flow. In order to represent 'ageing' effects on the deposit dynamics, we make use of a Coussot-type relation [15,16] that describes the evolution of the deposit rheology in terms of a competition between structuration and de-structuration, the latter being due to flow. This relation is an example of the simplest model that accounts for the jamming transition through temporal evolution of the deposit viscosity, which is based on thixotropic ideas [17,18]. Using this relation, it is possible to model the transition from a liquid-like to solid-like behaviour, incorporating both gradual and apparently catastrophically fast variations.

The deposition processes is modelled using a Stefan-like flux, which is linked to the thermodynamics underlying the phase separation process. In the present paper, this was based on a model for wax deposition in oil pipelines [19], which treats the oil flowing through the pipelines as a three-phase (vapour, liquid and solid) mixture of n hydrocarbon components. This model was selected since it provides a general framework for predicting the deposition of each of the n components through a phase transition, which ultimately depends on the local temperature field; the latter is coupled to the flow field through the energy conservation equation. Here, we consider a bi-component mixture for illustrative purposes.

We also use asymptotic reduction and integral theory, in conjunction with appropriate closure relations, in order to simplify the governing equations of mass, momentum and energy conservation and derive a set of evolution equations that describe the flow. This approach is common in modelling the hydrodynamics of thin films falling under the action of gravity or flowing over rapidly rotating surfaces [10], [20–24] and for two-layer channel flows [25]. It has also been used to model heated and reactive falling films [26,27]. This approach is a combination of boundary-layer theory and the Kármán–Pohlhausen averaging method [20,28], where the pressure is due to capillarity. Methods based on this approach require closure relations for the velocity, the most common of which

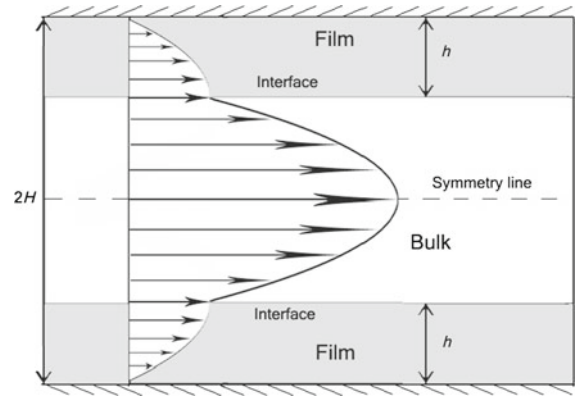

Fig. 1 Schematic of the two-fluid channel flow

correspond to semi-parabolic distributions that satisfy no-slip at the underlying wall and the shear-stress condition at the interface [20]. For non-isothermal problems, closures for the temperature field are also required, which are chosen to satisfy the boundary conditions at the wall and interface identically in some cases [27], and as part of the averaging procedure in others [23]. These approaches have been successful in capturing both the qualitative and, often quantitative, features of the interfacial waves formed, and have led to predictions which are in good agreement with experimental data [20,22,29]. In the present problem, closure relations are also required for the variable that parameterises the degree of structuration in the deposit.

We carry out a parametric study to elucidate the effect of ageing and deposition on the interfacial dynamics. For the case of ageing and no-deposition, we demonstrate that for certain parameter ranges, rapid ageing of the deposit can lead to the formation of steep waves and what appears to be finite-time 'blow-up' in the deposit thickness. In the presence of both ageing and deposition, we show the spatio-temporal evolution of the deposit and the rise in the deposition rate with temperature difference between the wall and the inlet.

The rest of this paper is organised as follows. In Sect. 2, we present a problem formulation, which leads to the derivation of the evolution equations governing the flow dynamics; details of the wall-deposition model are also provided. The results of our numerical simulations are presented in Sect. 3, and concluding remarks are provided in Sect. 4.

2 Problem formulation

2.1 Governing equations

We examine the dynamics of a two-dimensional, pressure-driven laminar two-fluid flow in a horizontal channel of height $2H$ and length L, as shown in Fig. 1. We assume the flow to be symmetric about the channel centerline and consider the case wherein a fast-moving core fluid flows past a much more viscous wall layer. Both layers are considered to be incompressible and the mechanism underlying the formation of the wall layer will be discussed below. We use a Cartesian coordinate system (x, z) to describe the dynamics where x and z denote the horizontal and vertical coordinates, respectively. The channel walls and interfaces are located at $z = (0, 2H)$ and $z = (h(x,t), 2H - h(x,t))$, respectively, where t denotes time. Due to the symmetry condition, which will be imposed at $z = H$, we will only consider the region $0 \leq z \leq H$. The channel walls will be considered smooth, rigid and impermeable and at a higher temperature than both that of the core fluid and wall layer.

For each fluid, conservation of mass, momentum and energy equations with appropriate boundary condition at the domain borders and interface are considered. For the core fluid, these equations are, respectively, expressed by

$$u_x + w_z = 0, \tag{1}$$

$$\rho(u_t + uu_x + wu_z) = -p_x + \mu(u_{xx} + u_{zz}), \tag{2}$$

$$\rho(w_t + uw_x + ww_z) = -p_z + \mu(w_{xx} + w_{zz}), \tag{3}$$

$$\rho C_p(T_t + uT_x + wT_z) = \kappa(T_{xx} + T_{zz}) + \mu\left(2\left[u_x^2 + w_z^2\right] + \left[u_z + w_x\right]^2\right), \tag{4}$$

where u, w, p, T, ρ, μ, C_p, and κ represent the horizontal and vertical components of the velocity, the pressure, temperature, density, viscosity, specific heat capacity at constant pressure, and the thermal conductivity, respectively. Here, we have neglected gravity and the effects of temperature on ρ, μ, C_p, and κ of the core fluid.

We suppose that the core fluid corresponds to a mixture of physically- and chemically-distinct components. Each one of these components is defined by its weight fraction, precipitation enthalpy, ΔH_{pi}, and precipitation point temperature, T_{pi}, which are input parameters. If $T > T_{pi}$ for a component i, then it will precipitate out of the core 'solution' creating a 'solid' phase and a mass flux, J, that depends on the local temperature gradient in the core fluid. A thermodynamic chemical equilibria model, described in Appendix, allows us to calculate the ratio between the 'solid' and liquid phases for each component in the core. The problem under consideration in the present work involves the continual deposition of the 'solid' phase at the wall to form the film, whose rheology will be described by (8); we focus below on the case of a bi-component mixture.

Using the chemical equilibria model, an estimate of the Stefan-like deposition flux, J, is obtained starting from Fick's law:

$$J = D_s \rho \frac{\eta}{T} T_n = D_s \rho \left[\frac{\eta}{T} \frac{(T_z - h_x T_x)}{\left(1 + h_x^2\right)^{1/2}}\right]_{z=h}, \tag{5}$$

where D_s is a diffusion coefficient and details of η, along with the derivation of J, are given in Appendix. Equation (5) represents the diffusive flux that arises as a result of phase separation, which results in the formation of a wall deposit. Note that T_n represents the normal derivative of the temperature. The flux J will feature in the interfacial boundary conditions which will be discussed below.

We will consider situations in which the wall layer undergoes an 'ageing' process. A rheological model has been adopted to take into account the variation of viscosity which depends on the flow history [15,16]:

$$\mu_f = \frac{\tau}{\dot{\gamma}} = \mu_0(1 + \lambda^n). \tag{6}$$

Here, the apparent viscosity of the wall layer, μ_f, is the ratio of shear stress, τ, to the second invariant of the rate of strain tensor given by

$$\dot{\gamma} = \left\{\frac{1}{2}\left[4\left(u_{f_x}\right)^2 + 4\left(w_{f_z}\right)^2 + 2\left(w_{f_x} + u_{f_z}\right)^2\right]\right\}^{\frac{1}{2}}, \tag{7}$$

where λ is the so-called structure parameter, μ_0 and n are fluid parameters; the subscript 'f' will be used below to designate quantities associated with the wall layer. We adopt the following form for the equation that governs the evolution of the structure parameter [14,16]

$$\lambda_t = \frac{1}{\Theta} - \alpha\lambda\left|\dot{\gamma}\right|, \tag{8}$$

in which α is a function of material characteristics and Θ is a characteristic time of 'restructuration' of the wall layer material. This layer will be referred to henceforth as the 'film'. Equation (8) is the simplest model that accounts for the temporal evolution of the deposit viscosity [17,18] allowing us to model the transition from liquid-like to solid-like behaviour either gradually or abruptly via variations of the parameters n, α and θ.

The mass, momentum and energy-conservation equations for the film are then, respectively, expressed by

$$u_{fx} + w_{fz} = 0, \tag{9}$$

$$\rho_f(u_{ft} + u_f u_{fx} + w_f u_{fz}) = -p_{fx} + 2\left[\mu_f u_{fx}\right]_x + \left[\mu_f\left(u_{fz} + w_{fx}\right)\right]_z, \tag{10}$$

$$\rho_f(w_{ft} + u_f w_{fx} + w_f w_{fz}) = -p_{fz} + \left[\mu_f\left(u_{fz} + w_{fx}\right)\right]_x + 2\left[\mu_f w_{fz}\right]_z, \tag{11}$$

$$\rho_f C_{pf}(T_{ft} + u_f T_{fx} + w_f T_{fz}) = \kappa_f(T_{fxx} + T_{fzz}) + \mu_f\left[2\left(u_{fx}^2 + w_{fz}^2\right) + \left(u_{fz} + w_{fx}\right)^2\right]. \tag{12}$$

2.2 Boundary conditions

The above governing equations are solved subject to the boundary conditions outlined below. We impose symmetry conditions at the channel centreline, $z = H$, which are expressed as follows:

$$u_z = w = T_z = 0. \tag{13}$$

We introduce boundary conditions, which have previously been used in the literature to model flows involving phase changes [8,10], [30–32]. We use a Stefan condition at the interface in order to relate the mass flux, J, to the difference in the velocity of the fluids on either side of the interface to that of the interface:

$$(u - u_f)h_x - (w - w_f) = J\left(\frac{1}{\rho_f} - \frac{1}{\rho}\right). \tag{14}$$

We also impose a jump condition for the energy at $z = h(x, t)$

$$\frac{1}{2}J^3\left(\frac{1}{\rho^2} - \frac{1}{\rho_f^2}\right) + \kappa_f\left(\frac{-T_{f_x}h_x + T_{f_z}}{\left(1+h_x^2\right)^{\frac{1}{2}}}\right) - \kappa\left(\frac{-T_x h_x + T_z}{\left(1+h_x^2\right)^{\frac{1}{2}}}\right)$$
$$+J\frac{2\mu_f}{\rho_f}\left[\frac{w_{f_z} + u_{f_x}h_x^2 - h_x(u_{f_z} + w_{f_x})}{\left(1+h_x^2\right)}\right] - J\frac{2\mu}{\rho}\left[\frac{w_z + u_x h_x^2 - h_x(u_z + w_x)}{\left(1+h_x^2\right)}\right] = 0, \tag{15}$$

and an interfacial no-slip condition:

$$(u_f - u) + (w_f - w)h_x = 0. \tag{16}$$

Normal-stress and tangential-stress conditions are imposed at $z = h(x, t)$, respectively, given by

$$p - p_f + \frac{J}{\left(1+h_x^2\right)^{\frac{1}{2}}}[w_f - w - h_x(u_f - u)] + \frac{2\mu_f}{\left(1+h_x^2\right)}\left[w_{fz} - u_{fx}h_x^2 - h_x(u_{fz} + w_{fx})\right]$$
$$-\frac{2\mu}{\left(1+h_x^2\right)}\left[w_z + u_x h_x^2 - h_x(u_z + w_x)\right] = \frac{\sigma h_{xx}}{\left(1+h_x^2\right)^{\frac{3}{2}}}, \tag{17}$$

$$\mu\left[(u_z + w_x)\left(1 - h_x^2\right) + 2h_x(w_z - u_x)\right] - \mu_f\left[(u_{fz} + w_{fx})\left(1 - h_x^2\right) + 2h_x(w_{fz} - u_{fx})\right] = \frac{(\sigma_x + h_x\sigma_z)}{\left(1+h_x^2\right)^{\frac{1}{2}}}. \tag{18}$$

We also impose a kinematic boundary condition at the interface which, after making use of (14), becomes

$$\frac{(h_t + u_f h_x - w_f)}{\left(1+h_x^2\right)^{\frac{1}{2}}} + \frac{J}{\rho_f} = 0 \quad \text{or} \quad \frac{(h_t + uh_x - w)}{\left(1+h_x^2\right)^{\frac{1}{2}}} + \frac{J}{\rho} = 0. \tag{19}$$

Finally, continuity of the temperature at $z = h(x, t)$ is also imposed. In the above conditions, σ is the interfacial tension, which depends on the temperature through the following linear relation $\sigma = \left[\sigma_w - \gamma\,(T - T_w)\right]$ in which σ_w denotes the interfacial tension at the wall, T_w.

In addition to the above interfacial conditions, we also impose no-slip and no-penetration conditions at $z = 0$,

$$u_f = w_f = 0, \tag{20}$$

and take the wall to be highly conducting:

$$T_f = T_w. \tag{21}$$

It is straightforward to extend the model to account for finite wall conductivity and finite wall thickness. We turn our attention to the scaling next.

2.3 Scalings

The above equations and boundary conditions are rendered dimensionless using the following scaling:

$$x = L\bar{x},\ (z,h) = H(\bar{z},\bar{h}),\ (w,w_f) = \epsilon V(w,\bar{w_f}),\quad t = \frac{L}{V}\bar{t}, \sigma = \sigma_w\bar{\sigma},\quad (p,p_f) = \frac{\mu V L}{H^2}(\bar{p},\bar{p_f}),$$
$$J = \epsilon\rho V\bar{J},\ \ (T,T_f) = (T_w - T_{\text{in}})\,(\bar{T},\bar{T}_f) + T_{\text{in}},\ \ \Theta = \bar{\Theta}\frac{L}{V}, \tag{22}$$

where overbars denote dimensionless quantities. Here, T_{in} is the temperature of the core fluid at the channel inlet, while V is the superficial velocity of the core fluid, and L is a characteristic length scale of an emergent coherent wave structure. The parameter $\epsilon \equiv H/L \ll 1$ is the aspect ratio of the coherent structure, assumed to be small and will be used as the basis for the perturbation expansion leading to the asymptotic reduction that will be carried out below [10]. Inserting this scaling into the system of equations in the previous sub-section yields (after dropping the bars)

$$u_x + w_z = 0, \tag{23}$$
$$\epsilon\text{Re}(u_t + uu_x + wu_z) = -p_x + \epsilon^2 u_{xx} + u_{zz}, \tag{24}$$
$$\epsilon\text{Re}(w_t + uw_x + ww_z) = -\frac{p_z}{\epsilon^2} + \epsilon^2 w_{xx} + w_{zz}, \tag{25}$$
$$\epsilon\text{Re}\,\text{Pr}(T_t + uT_x + wT_z) = \epsilon^2 T_{xx} + T_{zz} + \epsilon^2\text{Br}\left[2\left(u_x^2 + w_z^2\right) + \left(\frac{u_z}{\epsilon} + \epsilon w_x\right)^2\right], \tag{26}$$
$$u_{f_x} + w_{f_z} = 0, \tag{27}$$
$$\frac{\epsilon m\text{Re}}{r_d}(u_{f_t} + u_f u_{f_x} + w_f u_{f_z}) = -mp_{f_x} + 2\epsilon^2\left[(1+\lambda^n)u_{f_x}\right]_x + \left[(1+\lambda^n)(u_{f_z} + \epsilon^2 w_{f_x})\right]_z, \tag{28}$$
$$\frac{\epsilon m\text{Re}}{r_d}(w_{f_t} + u_f w_{f_x} + w_f w_{f_z}) = -\frac{m}{\epsilon^2}p_{f_z} + \left[(1+\lambda^n)\left(u_{f_z} + \epsilon^2 w_{f_x}\right)\right]_x + 2\epsilon^2\left[(1+\lambda^n)w_{f_z}\right]_z, \tag{29}$$
$$\frac{\epsilon r_k}{r_d r_{Cp}}\text{Re}\,\text{Pr}(T_{f_t} + u_f T_{f_x} + w_f T_{f_z}) = \epsilon^2 T_{f_{xx}} + T_{f_{zz}} + \frac{\epsilon^2 r_k\text{Br}}{m}(1+\lambda^n)\left[2\left(u_{f_x}^2 + w_{f_z}^2\right) + \left(\frac{u_{f_z}}{\epsilon} + \epsilon w_{f_x}\right)^2\right], \tag{30}$$
$$\lambda_t = \frac{1}{\Theta} - \frac{\alpha\lambda\left|u_{f_z}\right|}{\epsilon}. \tag{31}$$

The dimensionless interfacial conditions become

$$\epsilon\left(u - u_f\right) - \epsilon\left(w - w_f\right) = \bar{J}\,(r_d - 1), \tag{32}$$
$$\frac{1}{2}\text{ReBr}J^3\,(1 - r_d) + \frac{1}{r_k}\left(\frac{+T_{f_z} - \epsilon^2 T_{f_x}h_x}{\left(1+\epsilon^2 h_x^2\right)^{\frac{1}{2}}}\right) - \left(\frac{+T_z - \epsilon^2 T_x h_x}{\left(1+\epsilon^2 h_x^2\right)^{\frac{1}{2}}}\right)$$
$$+2J\text{Br}\left[\frac{r_d\epsilon}{m}\left(1+\lambda^n\right)\frac{\left[w_{f_z} + \epsilon u_{f_x}h_x^2 - h_x\left(u_{f_z} + \epsilon^2 w_{f_x}\right)\right]}{\left(1+\epsilon^2 h_x^2\right)} - \frac{\left[w_z + \epsilon u_x h_x^2 - h_x\left(u_z + \epsilon^2 w_x\right)\right]}{\left(1+\epsilon^2 h_x^2\right)}\right], \tag{33}$$
$$\left(u_f - u\right) - \epsilon^2\left(w_f - w\right)h_x = 0, \tag{34}$$
$$p - p_f + \frac{\epsilon^2\text{Re}J}{\left(1+h_x^2\right)^{\frac{1}{2}}}[w_f - w - h_x(u_f - u)] + \frac{2\epsilon^2(1+\lambda^n)}{m\left(1+h_x^2\right)}\left[w_{f_z} - h_x u_{f_z} + \epsilon^2\left(u_{f_x}h_x^2 - h_x w_{f_x}\right)\right]$$
$$-\frac{2\epsilon^2}{\left(1+h_x^2\right)}\left[w_z - h_x u_z + \epsilon^2\left(u_x h_x^2 - h_x w_x\right)\right] = \frac{\epsilon^3}{\text{Ca}}\frac{h_{xx}}{\left(1+h_x^2\right)^{\frac{3}{2}}}\left[1 - \gamma\,(T-1)\right], \tag{35}$$
$$\left(u_z + \epsilon^2 w_x\right)\left(1 - \epsilon^2 h_x^2\right) + 2\epsilon^2 h_x(w_z - u_x) - \frac{(1+\lambda^n)}{m}\left(u_{f_z} + \epsilon^2 w_{f_x}\right)\left(1 - \epsilon^2 h_x^2\right) + 2\epsilon^2 h_x(w_{f_z} - u_{f_x})$$
$$= -\frac{\epsilon\left(1+\epsilon^2 h_x^2\right)^{\frac{1}{2}}}{\text{Ca}}\left[\gamma\,(T_x + h_x T_z)\right], \tag{36}$$

$$\frac{\epsilon(h_t + u_f h_x - w_f)}{\left(1+\epsilon^2 h_x^2\right)^{\frac{1}{2}}} + r_d J = 0, \quad \text{or} \quad \frac{\epsilon(h_t + u h_x - w)}{\left(1+\epsilon^2 h_x^2\right)^{\frac{1}{2}}} + J = 0, \tag{37}$$

$$T = T_f. \tag{38}$$

The symmetry conditions at the centreline, and the no-slip and no-penetration conditions at the channel wall remain unaltered. The temperature condition at the wall becomes

$$T_f = 1. \tag{39}$$

The dimensionless flux, J, is given by

$$J = \frac{1}{\mathrm{Pe}}\left[\frac{\eta}{(T+\Gamma)}T_z\right]_{z=h}, \tag{40}$$

in which η is given in Appendix and $\Gamma \equiv \frac{T_{\mathrm{in}}}{\Delta T}$ wherein $\Delta T \equiv T_w - T_{\mathrm{in}}$.

In the above equations and boundary conditions, the following dimensionless parameters have been introduced:

$$\mathrm{Re} \equiv \frac{\rho V H}{\mu}, \quad \mathrm{Pr} \equiv \frac{C_{Pb}\mu}{\lambda}, \quad \mathrm{Pe} \equiv \frac{LV}{D_s}, \quad \mathrm{Br} \equiv \frac{\mu V^2}{k\Delta T}, \tag{41}$$

where Re, Pr and Br, are the Reynolds, Prandtl, and Brinkman numbers. In addition, we introduce the following ratios:

$$m \equiv \frac{\mu}{\mu_0}, \quad r_d \equiv \frac{\rho}{\rho_f}, \quad r_{Cp} \equiv \frac{C_P}{C_{Pf}}, \quad r_\kappa \equiv \frac{\kappa}{\kappa_f}. \tag{42}$$

2.4 Rescaling

We now consider situations in which there is a large disparity between the viscosities of the core fluid and wall layer, so that $m \ll 1$. This is consistent with the motivating engineering application mentioned in the Introduction, crude-oil fouling, wherein the foulant corresponds to a highly viscous wall layer. We exploit this feature of the flow in order to simplify the governing equations and boundary conditions by introducing the following rescalings [25]

$$(u_f, w_f) = m(\tilde{u_f}, \tilde{w}_f), \quad t = \frac{\tilde{t}}{m}, \quad \mathrm{Re} = \frac{\tilde{\mathrm{Re}}}{\epsilon}, \quad \mathrm{Ca} = \epsilon^3\tilde{\mathrm{Ca}}, \quad \mathrm{Pe} = \frac{\tilde{\mathrm{Pe}}}{\epsilon}, \quad \Theta = \frac{\tilde{\Theta}}{m}, \quad \alpha = \epsilon\tilde{\alpha}. \tag{43}$$

The dimensionless leading-order equations then reduce to

$$u_x + w_z = 0, \ \mathrm{Re}(uu_x + wu_z) = -p_x + u_{zz} + O(\epsilon), \quad p_z = 0 + O(\epsilon), \tag{44}$$

$$\mathrm{RePr}(uT_x + wT_z) = T_{zz} + O(\epsilon), \tag{45}$$

$$u_{f_x} + w_{f_z} = 0, \quad pf_x = \left[(1+\lambda^n)u_{f_z}\right]_z + O(\epsilon^2), \quad p_{f_z} = 0 + O(\epsilon^2), \tag{46}$$

$$T_{f_{zz}} = 0 + O(\epsilon^2), \tag{47}$$

$$\lambda_t = \frac{1}{\Theta} - \alpha\lambda\left|u_{f_z}\right|. \tag{48}$$

The interfacial conditions reduce to

$$\left(u - u_f\right) - \left(w - w_f\right) = J\left(r_d - 1\right), \quad u = w = 0 + O(\epsilon^2), \tag{49}$$

$$p = p_f + \frac{h_{xx}}{\mathrm{Ca}} + O(\epsilon), \quad u_z = (1+\lambda^n)u_{f_z} + O(\epsilon), \quad h_t + uh_x - w + r_d J = 0, \tag{50}$$

$$T_{f_z} = r_k T_z + O(\epsilon^2), \quad T = T_f. \tag{51}$$

The symmetry conditions at $z = 1$ and the no-slip and no-penetration conditions at $z = 0$ remain unaltered.

2.5 Lubrication theory and the integral method

Here, we derive evolution equations that govern the dynamics of the flow by employing lubrication theory for the wall layer, and a combination of boundary-layer theory and an averaging procedure for the core fluid [20,21,25]; the latter requires closure relations for the velocity and temperature fields, and the structure parameter λ, as will be discussed below. We start by re-expressing the kinematic boundary condition as

$$h_t + \left[\int_0^h (h - z) u_{fz} \mathrm{d}z \right]_x + r_d J = 0, \tag{52}$$

in which u_{fz} is obtained via integration of the x-component of the momentum conservation equation in the film and application of the tangential-stress condition at $z = h(x, t)$:

$$u_{f_z} = \frac{p_{f_x}(z - h) + \tau_i}{(1 + \lambda^n)}. \tag{53}$$

Here, $u_z(z = h) \equiv \tau_i$ denotes the interfacial tangential-stress. Integration of the x-component of the Navier–Stokes equations in the core fluid yields

$$\mathrm{Re} \left(\int_h^1 u^2 \mathrm{d}z \right)_x + p_x(1 - h) + \tau_i = 0. \tag{54}$$

Progress is made by choosing the following closure relation for u, which satisfies $u = 0$ at $z = h$, $u_z = 0$ at $z = 1$, and $\int_h^1 u \mathrm{d}z = 1/2$ [25]:

$$u = \frac{3}{4(h - 1)^3} \left[z^2 - 2z - h(h - 2) \right]. \tag{55}$$

This closure yields the following expression for the interfacial stress

$$\tau_i = \frac{3}{2(h - 1)^2}. \tag{56}$$

Substitution of Eqs. (55) and (56) in Eq. (54) yields the following expression for the pressure gradient in the core

$$p_x = \frac{3}{10(h - 1)^3} (5 + h_x \mathrm{Re}). \tag{57}$$

From the leading-order normal-stress jump condition at $z = h(x, t)$ we obtain the pressure gradient in the film:

$$p_{fx} = \frac{3}{10(h - 1)^3} (5 + h_x \mathrm{Re}) - \frac{h_{xxx}}{\mathrm{Ca}}. \tag{58}$$

Substitution of (56) and (58) in (53) and the resultant equation in (52) finally yields an evolution equation for $h(x, t)$:

$$h_t + \left[\int_0^h \left\{ \frac{15\mathrm{Ca}(h - z)(h - 1) - (h - z)^2 \left[3\mathrm{Ca}\,(5 + h_x \mathrm{Re}) - 10 h_{xxx} (h - 1)^3 \right]}{10\mathrm{Ca}(1 + \lambda^n)(h - 1)^3} \right\} \mathrm{d}z \right]_x + r_d J = 0. \tag{59}$$

For the core fluid temperature, we adopt the following closure, which satisfies continuity of temperature at $z = h(x, t)$ and the symmetry condition at $z = 1$:

$$T = A(z^2 - h^2) - 2A(z - h) + 2Ar_k(h - 1)h + 1. \tag{60}$$

It is possible to derive the following expression for T_f via integration of the leading-order energy equation in the film and application of the thermal condition at the wall and the thermal flux condition at $z = h(x, t)$:

$$T_f = 2Ar_k(h - 1)z + 1. \tag{61}$$

Integration of the leading order energy equation in the core gives

$$\mathrm{RePr}\left[\int_h^1 uT\,\mathrm{d}z\right]_x = -T_z\,|_h, \tag{62}$$

and substitution of (60) in (62) yields the following equation for the function $A(x,t)$

$$\frac{\mathrm{RePr}}{5}\left((h-1)\left(2+(5r_k-2)\,h\right)A_x + A\left(4-5r_k+2\left(5r_k-2\right)h\right)h_x\right) + 2A(h-1) = 0. \tag{63}$$

For λ, we choose the following closure

$$\lambda = \lambda_w \frac{(z-h)^2}{h^2}, \tag{64}$$

where $\lambda_w(x,t)$ represents the spatio-temporally varying value of λ along the channel wall. This closure satisfies the conditions $\lambda = \lambda_z = 0$ at $z = h(x,t)$: here, we suppose that interfacial stress will lead to destruction of the internal structure of the wall layer; consequently, λ would be expected to be largest at the wall. This is supported by the results of full-scale numerical simulations of the governing equations using the diffuse-interface method [33]. Substitution of (53) and (64) in (31) yields the following evolution equation for λ_w:

$$\lambda_{wt} = \frac{1}{h}\left[3\left(\frac{h}{\Theta} - I\right) - \lambda_w h_t\right]; \tag{65}$$

here, $I \equiv \alpha \int_0^h \lambda \left|u_{fz}\right| \mathrm{d}z$. Equations (59), (63) and (65) are fully coupled to the flux J; an expression for J is obtained following the substitution of (60) in (40). We turn our attention to the presentation of the results next.

3 Results

In this section, we provide a discussion of our results. We begin, however, with a short description of the numerical procedure employed to carry out the computations and of the initial and boundary conditions used for h, A, and λ_w.

3.1 Numerical procedure

The evolution of the flow is studied via numerical solution of (59), (63) and (65). The flux, J, is given by (40) with $T(x, z = h, t) = 2Ar_k(h-1) + 1$ and $T_z(x, z = h, t) = 2A(h-1)$. We consider the case wherein the core fluid corresponds to a bi-component mixture for which η is given by (93) (and associated relations). We fix the values of the following parameters $M_1 = M_2 = 100$ kg/kmol, $K_{10} = K_{20} = \beta_1 = \beta_2 = 1, z_1 = z_2 = 0.5$, $\mathrm{Pe} = 10^4$, $T_{p1} = T_{p2} = 373\ K$, $T_{\mathrm{in}} = 473\ K$; the latter temperatures lead to $\Omega_1 = \Omega_2 = 1.27$. We also fix $\mathrm{Ca} = 1$, $\mathrm{Pr} = 100$, $r_d = r_{Cp} = 1$, $r_\kappa = 0.1$, and $\alpha = 3$ [11]. One expects that increasing the value of T_w decreases Γ thereby increasing K_i and, ultimately, J; this leads to an increase in the deposition rate. One also expects the deposition and ageing effects to be mitigated by the interfacial interactions whose intensity will increase with Re, while ageing will be promoted by decreasing Θ and n. Below, we will, therefore, investigate the effect of varying Re, Θ, Γ, and n on the dynamics.

We use a numerical procedure that employs finite-element collocation to discretise the spatial derivatives and Gear's method to advance the solution in time [34]; this has been used previously to simulate related thin-film flows [22,25,35,36]. Numerical solutions are obtained for domain lengths $\mathcal{L} = 300$ with 1000-3000 grid points starting from the following initial conditions:

$$h(x,0) = h_o[1 + 0.01 \times \exp(-10[x-5]^2)], \tag{66}$$

$$A(x,0) = A_0 \exp\left[-10x/\left(2 + [5r_\kappa - 2]h_o\right)/\mathrm{RePr}\right], \tag{67}$$

$$\lambda_w(x,0) = 0, \tag{68}$$

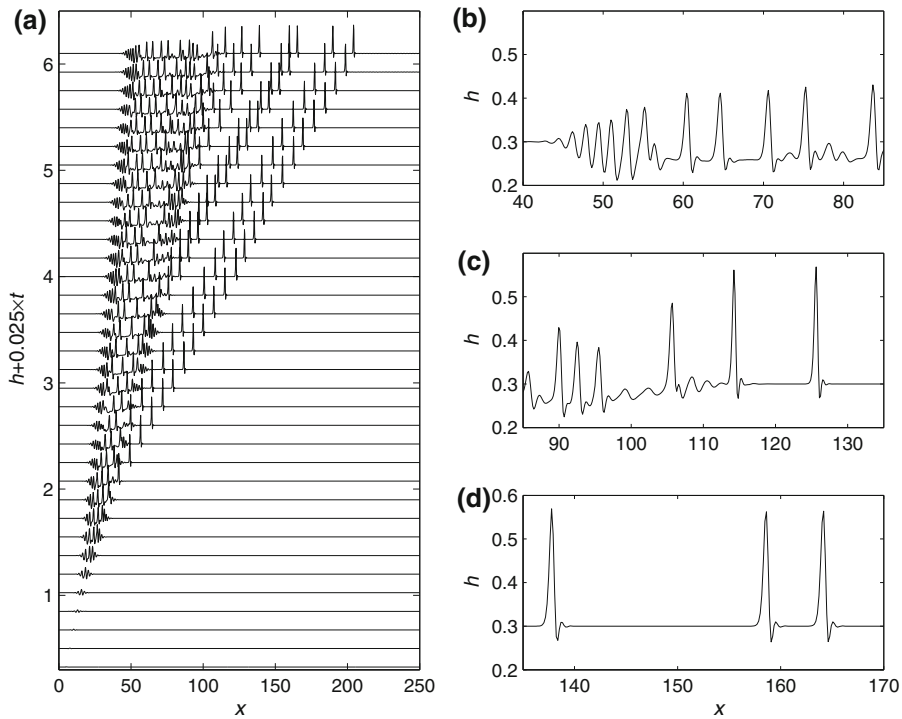

Fig. 2 Interfacial dynamics in the absence of ageing and wall deposition with Re $= 20$, Ca $= 1$ and $h_o = 0.3$. Panel **a** shows a space–time plot of h; **b**–**d** depict the h profile over three different x intervals for $t = 43.46$

which correspond to an initially uniform film, except for a very small perturbation, $0.01h_o \times \exp(-10[x-5]^2)$, with constant viscosity, having $\lambda = 0$. Equation (67) is obtained from (63) with $h = h_o$; here, A_0 is given by

$$A_0 = \frac{3}{2(1-h_o)(1+[3r_\kappa - 1]h_o)}, \tag{69}$$

which was obtained by demanding that the average core temperature at $x = 0$ equals $T_{\text{in}} : (1/(1-h_o)) \int_{h_o}^{1} T\,\mathrm{d}z = 0$. The numerical solutions are subject to the following boundary conditions

$$(h, h_{xxx})(0,t) = (h_o, 0), \quad A(0,t) = A_0, \quad \lambda_w = 0, \tag{70}$$

$$(h_x, h_{xxx})(\mathcal{L},t) = 0, \quad A_x(\mathcal{L},t) = 0, \quad \lambda_w = 0. \tag{71}$$

3.2 Discussion

3.2.1 No-ageing and no-deposition

We begin the discussion of our results by first examining the flow in the absence of deposition and ageing effects. This situation is recovered in the limits $(\alpha, \Theta, \text{Pe}) \to (0, \infty, \infty)$. We show in Fig. 2 the interfacial dynamics that accompany the flow for Re = 20, which were studied by Matar et al. [25]; these authors also studied the effect of Re and h_o on the wave dynamics, and their results will be not reproduced here. It can be seen from Fig. 2, which represents a space–time plot of h, that disturbances are convected away from the channel inlet and develop into a wavepacket, which then begins to radiate large-amplitude waves. It is possible to discern four regions at the interface in the latest snapshot shown in the space–time plot (at $t = 43.46$); these will be referred to below as regions '1–4', respectively.

There is a region near the inlet, which is seemingly uniform in thickness although it is populated by waves of small-amplitude that are convected downstream. This is then followed by a region comprising a thin strip over which the waves that are convected from the inlet region develop into waves of large amplitude. This is shown in Fig. 2b where the 'nucleation' of waves between the large-amplitude waves can also be discerned; the average film thickness in this region also decreases due to the increase in its average velocity, which is brought about by the wave-formation. The average film thickness then increases over another transition region, shown in Fig. 2c, in which the large-amplitude waves give way to solitary pulses, which then accelerate away from this region and populate regions downstream (see Fig. 2d). Inspection of Fig. 2a also shows that the extent of region '1' grows relatively slowly with time; this is far exceeded by the rate of propagation of the waves in regions '2' and '3' in the middle of the domain, which, in turn, is exceeded by that of the solitary pulses in region '4'. As also shown by Matar et al. [25], decreasing the value of Re and/or h_0 yields a situation in which a wavepacket forms and travels downstream and eventually exits the right-hand boundary leaving behind a waveless film.

3.2.2 Effect of ageing

We turn our attention to investigating the flow in the presence of ageing by first considering the waveless, steady case and its linear stability. It is possible to derive a waveless steady-state solution for λ_w, λ_{ws}, by setting the time-derivatives in (59) and (65), which yields

$$\frac{h_s}{\Theta} - \frac{3\alpha h_s \lambda_{ws}}{2(h_s-1)^3}\int_0^1 \frac{(\eta h_s - 1)(\eta-1)^2}{(1+\lambda_{ws}^n(\eta-1)^{2n})}\mathrm{d}\eta = 0, \tag{72}$$

where $\eta = z/h_s$. Solution of this equation yields λ_{ws} given h_s and n.

It is also possible to consider the situation in which the magnitude of λ_w is small so that (59) and (65) may be linearised to yield

$$h_t + \left(\frac{h^2}{60}\left[4h(3\lambda_w - 5)p_{fx} - 15(\lambda_w - 2)\tau_i\right]\right)_x = 0, \tag{73}$$

$$\lambda_{wt} \approx \frac{3}{\Theta} - \alpha\lambda_w\left(\tau - \frac{3}{4}hp_{fx}\right) - \lambda_w\frac{h_t}{h}. \tag{74}$$

A linear stability analysis of these equations can be carried out using normal modes:

$$(h, \lambda_w) = (h_s, \lambda_{ws}) + (\hat{h}, \hat{\lambda_w})\exp(\mathrm{i}kx + \omega t). \tag{75}$$

Here, $(\hat{h}, \hat{\lambda_w})$ represent linear perturbations to the steady-state values of h and λ_w, given by h_s and λ_{ws}, respectively; k and ω denote the disturbance (real) wavenumber and (complex) growth rate. The steady solution, λ_{ws}, can be obtained either via linearisation of (72) or following the omission of the time-derivatives in (73). An analytical expression for λ_{ws} is only possible for $n = 1$:

$$\lambda_{ws} = \frac{8(h_s-1)^3}{\alpha\Theta(h_s-4)}. \tag{76}$$

Note that the parameters α and Θ enter this equation as $\alpha\Theta$ and are no longer independent. Thus, an increase (decrease) in $\alpha\Theta$, which arises due to an increase (decrease) in α and/or Θ represents an increase (decrease) in the rate of de-structuration and a decrease (increase) in the structuration rate, which hinders (promotes) ageing.

Linearisation of (73) and (74) and subsequent solution of the characteristic equation for the eigenvalue ω yields a dispersion relation for the growth rate ω_r as a function of k. In Fig. 3a, we plot the variation of λ_{ws} with h_s, which shows that λ_{ws} increases with decreasing h_s, which illustrates that structure-building is more significant in thinner films. This increase becomes more pronounced with decreasing $\alpha\Theta$, as expected. Equation (76) was derived by assuming that λ_{ws} is small and this must be kept in mind when interpreting the trends exhibited in Fig. 3a where this assumption clearly fails (which is true for small h_s and $\alpha\Theta$). In Fig. 3b, we show the dispersion curves for

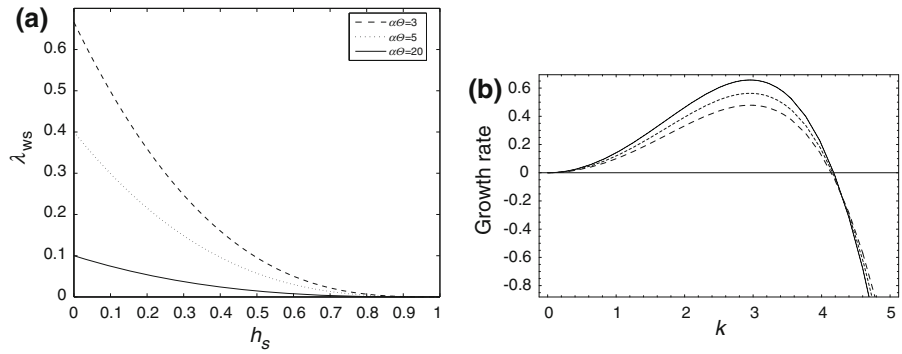

Fig. 3 The variation of λ_{ws} (Eq. (76)) with h_s (**a**), and the disturbance growth rate, ω_r, with k (**b**), for different values of $\alpha\Theta$, $n = 1$ and $h_s = 0.3$

$h_s = 0.3$ and three values of $\alpha\Theta$. The curves are paraboloidal with a range of wavenumbers, $0 < k < k_c$, for which $\omega_r > 0$ indicating the presence of a linear instability, promoted by inertia [25]. Inspection of this plot reveals that decreasing $\alpha\Theta$, which leads to larger λ_{ws} values, is stabilising, giving rise to a decrease in the growth rates for disturbances $0 < k < k_c$, and an increase in the decay rates for $k > k_c$.

The nonlinear interfacial dynamics are investigated next. We show in Fig. 4 a space–time plot for $\alpha = \Theta = n = 1$ with the rest of the parameters remaining unaltered from Fig. 2. It is seen that the h-dynamics are clearly similar to those in the absence of ageing, presented in Fig. 2: there is an almost-waveless inlet region, which is followed by a transition to large-amplitude waves, followed by another to form solitary pulses. The evolution of λ_w, shown in Fig. 5, demonstrates that λ_w also exhibits wave-formation due to its coupling to h. The magnitude of λ_w undergoes its largest decrease beneath the wave peaks, and is highest below the wave troughs. This is because the $|u_{fz}|$ is highest below the peaks and this promotes de-structuration, which acts to decrease λ_w.

We have also investigated the effect of varying Θ on the spatio-temporal dynamics of h and λ_w; this is shown in Fig. 6 for $\alpha = 1$ and the rest of the parameters remaining unchanged from Fig. 4. It is seen clearly that increasing Θ increases the time-scale for structuration and leads to small average λ_w values: the h profiles generated with $\Theta = 10$ (see Fig. 6g) are very similar to those obtained in the absence of ageing (see Fig. 6a). The structure of region '2' appears to be weakly dependent on variations in Θ, however, for the lowest Θ values investigated, regions '3' and '4' merge into a single region, populated by large-amplitude, solitary pulses. The average value of λ_w also follows that of h (a tentative indication of this has already been provided by Fig. 3a and Eq. (76)): it is lowest for thickest average h, which is in region '1' near the inlet, and highest for the thinnest average h, in region '4'; the steady values of λ_w in these regions were found to be in agreement with the predictions of (72).

As shown in the insets of Fig. 6c and d, although the value of h remains fixed at $h = h_o$ for $x = 0$, h increases in the region immediately adjacent to the inlet in order to accommodate the increase in the viscosity of the film due to structure-building in the wall layer; the film must thicken since its velocity decreases as a result of the viscosity build-up. With decreasing Θ, there is an increase in the average film thickness in the inlet region, brought about by the rapid increase in λ_w. The decrease in Θ also leads to retardation in the propagation rate of all waves due to the associated increase in viscous dissipation. Downstream of the inlet, the average film thickness decreases since its velocity increases in the region populated by waves. In the region further downstream, the average thickness remains below h_o and the film remains waveless, promoting structure build-up and an increase in λ_w.

In Fig. 7, we show the effect of varying n on the flow profiles for $\alpha = 1$ and $\Theta = 0.5$, and the rest of the parameters remaining unaltered. It is seen that decreasing the value of n leads to more regularly spaced, high-amplitude solitary pulses in h, which coincide with sharp depressions in λ_w, as shown in Fig. 7a and b. Regular waves in aged cornstarch suspensions, flowing down an incline, have been observed previously by Balmforth et al. [37]. Increasing n leads to the formation of less regularly spaced pulses in h and depressions in λ_w. For n=1, the solutions in $50 \leq x \leq 120$ resemble the 'bound-states' observed in other thin-film flows, namely those down a vertical fibre [38].

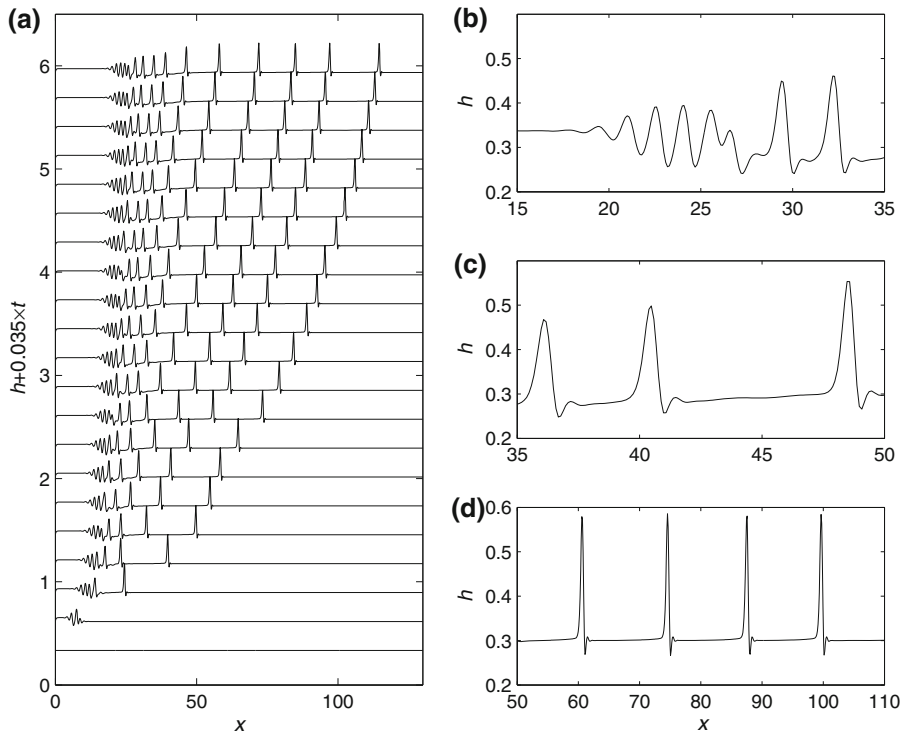

Fig. 4 Interfacial dynamics in the presence of ageing with $\alpha = \Theta = n = 1$ and the rest of the parameter values remaining unaltered from Fig. 2. Panel **a** shows a space–time plot of h; **b–d** depict the h profile over three different x-intervals for $t = 29.37$

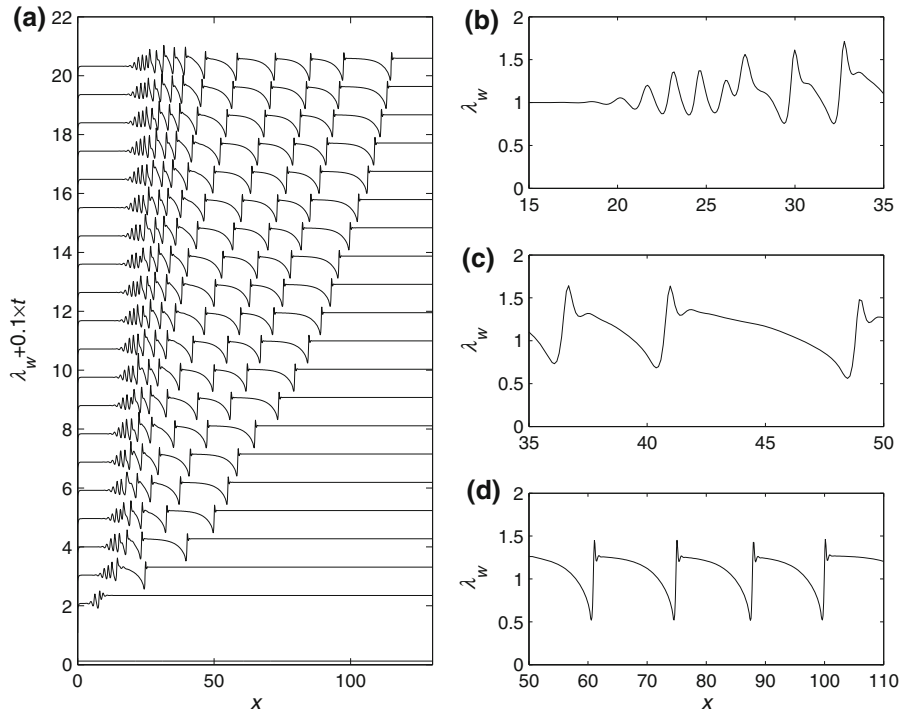

Fig. 5 Interfacial dynamics in the presence of ageing with $\alpha = \Theta = n = 1$ and the rest of the parameter values remaining unaltered from Fig. 2. Panel **a** shows a space–time plot of λ_w; **b–d** depict the λ_w profile over three different x-intervals for $t = 29.37$

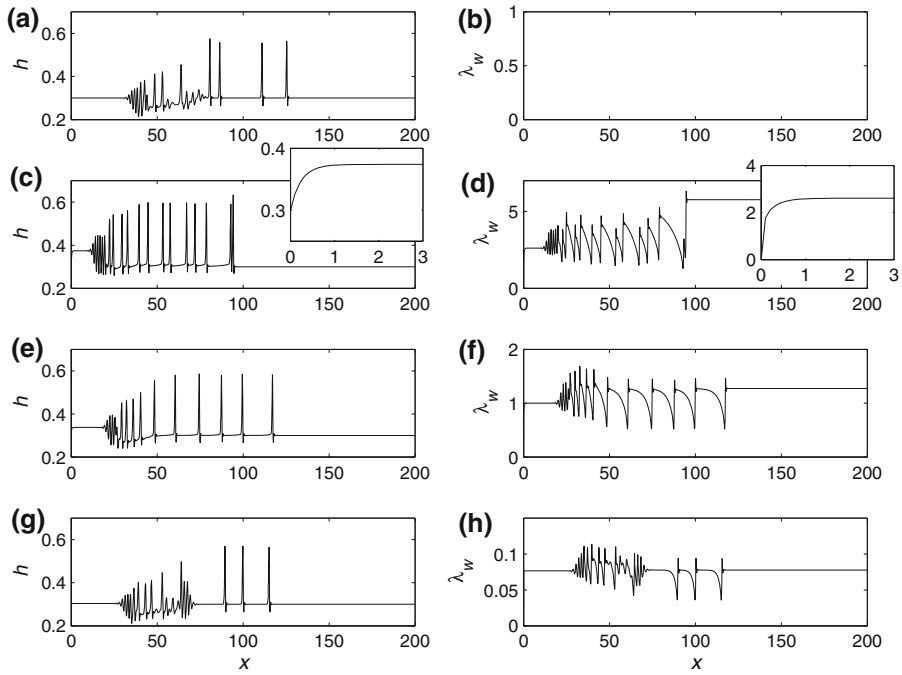

Fig. 6 The effect of varying Θ on the profiles of h and λ_w for $\Theta \to \infty$, and $\Theta = 0.5, 1, 10$ shown in panels (**a**, **b**)–(**g**, **h**), respectively, for $t = 29.4$. The *insets* in panels **c** and **d** show an enlarged view of the inlet region. The rest of the parameter values remain unaltered from Fig. 4

It may be possible to explain the presence of such states in the present set of equations through an analysis similar to that carried out by Duprat et al. whereby the separation of the pulses can be tracked as a parametric function of n for fixed Θ; however, this is beyond the scope of this paper.

A further increase in n to values above unity results in a transition from a dynamics accompanied by the continuous formation of solitary waves to one involving what appears to be finite-time 'blow-up' in h. Examples of this are shown in Fig. 7e, g, and i, which depict the final solution that can be calculated prior to 'blow-up'. These solutions are characterised by a wave with a large peak, which approaches the channel centreline. The development of these waves occurs at earlier times and at locations whose distance from the inlet decreases with increasing n; this is accompanied by a rapid build-up of λ_w, as shown in Fig. 7f, h, and j, corresponding to a rather abrupt change in the deposit rheology towards a solid-like behaviour.

The evolution of the interface towards 'blow-up' and the build-up in λ_w is shown in Fig. 8a and b for $n = 1.2$ with the rest of the parameters remaining unchanged from Fig. 7. It is seen clearly that interfacial waves are formed near the inlet region and propagate downstream. The interaction between successive waves results ultimately in their coalescence into a large-amplitude solitary wave, which gives rise to 'blow-up'; the latter is shown in Fig. 8c, together with the last profile λ_w prior to 'blow-up'. It is tempting to conclude that the behaviour shown in Figs. 7 and 8 heralds the onset of a 'bridging' event, whereby peaks from either side of the centreline meet. It is more likely, however, that the equations become deficient in the relevant physics required to regularise the solutions after the coalescence event, preventing the occurrence of 'blow-up'; similar 'blow-up' phenomena have been encountered previously in thin-film equations (e.g. the Benney equation [39]). It may be possible to regularise such models by replacing them with 'two-equation' models of which the Shkadov equations [20] (or those derived using the method of weighted residuals [40]) are an example; these models couple the interface equation to an evolution equation for the film flow rate.

We have also studied briefly the effect of initial degree of structuration on the dynamics, characterised by the initial, finite value of λ_w, $\lambda_w(x, 0)$. For the runs starting from $\lambda_w(x, 0) > 0$, the boundary condition on λ_w at $x = 0$

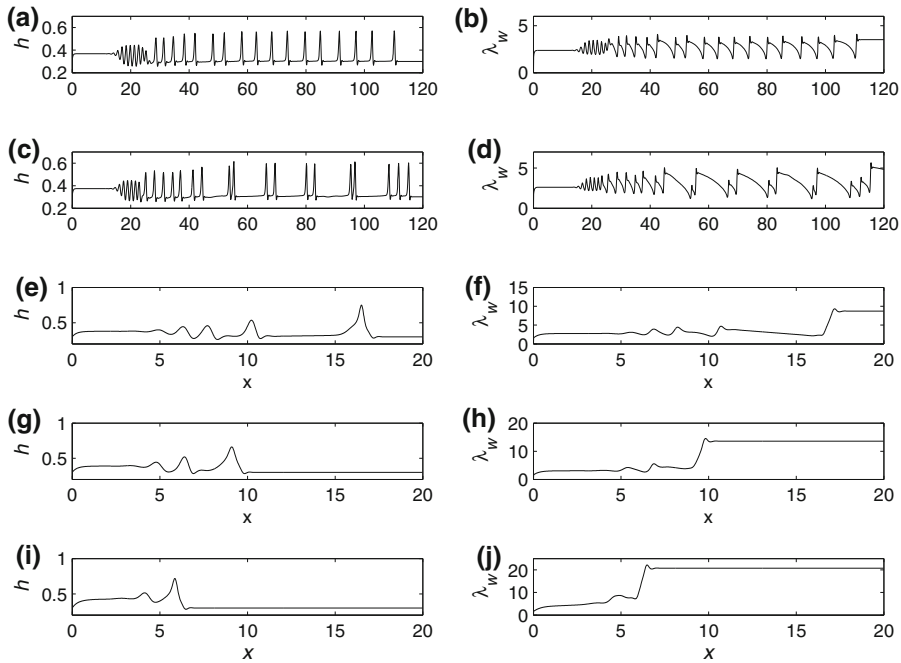

Fig. 7 The effect of varying n on the profiles of h and λ_w with $\Theta = 0.5$ and $n = 0.5,\ 1,\ 1.2,\ 1.5,\ 2$ shown in panels (**a**, **b**)–(**e**, **f**), respectively, for $t = 40.01,\ 40.08,\ 8.92,\ 6.98,\ 6.53$, respectively. The rest of the parameter values remain unaltered from Fig. 4

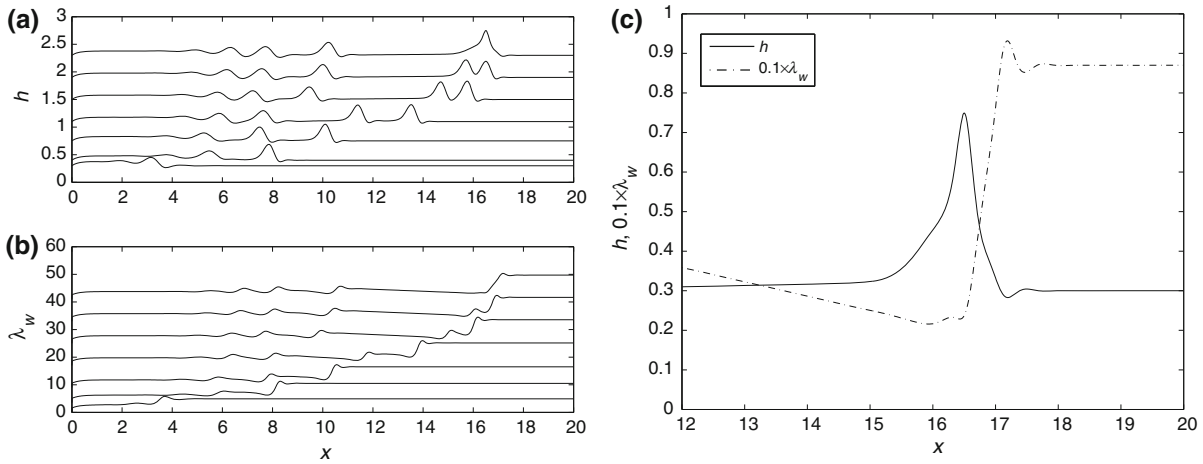

Fig. 8 The evolution towards 'blow-up' for $n = 1.2$ in h and λ_w shown in (**a**) and (**b**), respectively, for $t = 2.82, 5.66, 6.54, 7.81, 8.66, 8.89, 8.92$; an enlarged view of h and λ_w at $t = 8.92$ is shown in (**c**). The rest of the parameters remain unaltered from Fig. 7

is $\lambda_w(0, t) = \lambda_w(0, 0)$. Our results (not shown) indicate that similar 'blow-up' phenomena occur for a sufficiently large initial structuration level (e.g. with $\lambda_w(x, 0) = 100$ for $\alpha = \Theta = n = 1$, Ca $= 1$, and Re $= 20$).

The effect of Θ and n on an integral measure of the interfacial waviness, $W(t)$, which is expressed by

$$W(t) = \frac{\int_0^{\mathcal{L}} (h - h_o)^2 \mathrm{d}x}{\mathcal{L}}, \tag{77}$$

is shown in Fig. 9. Here, it can be seen that interfacial waviness is enhanced with decreasing Θ and increasing n, except for the case of $n = 2$ which ends abruptly for the reasons mentioned above. The results shown in Figs. 6–9

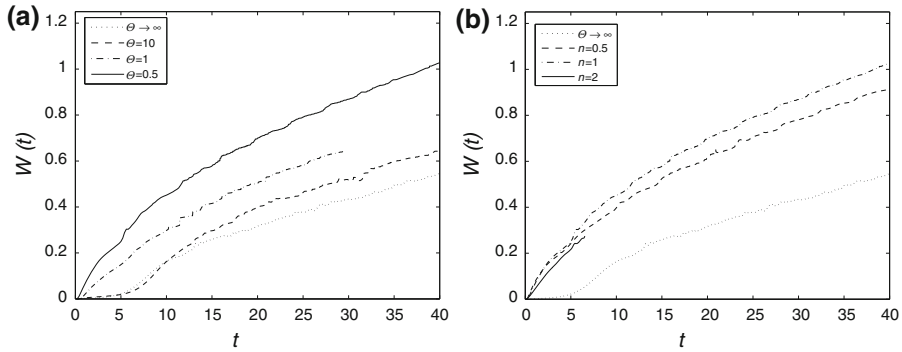

Fig. 9 The effect of varying Θ and n, shown in (**a**) and (**b**), respectively, on the integral measure of the interfacial waviness, W. Unless stated otherwise in the legend, $n = \Theta = 0.5$ and the rest of the parameter values remain unaltered from Fig. 4

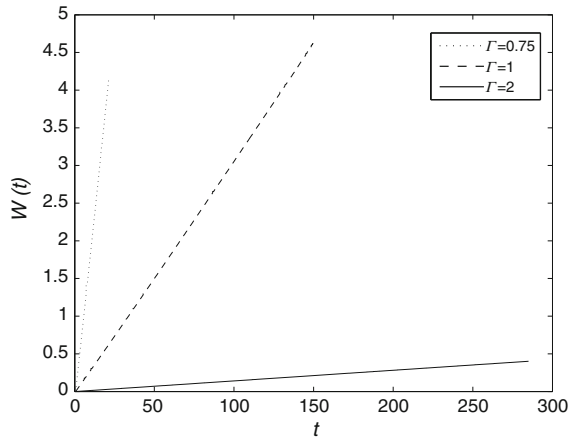

Fig. 10 The effect of varying Γ on the integral measure of the interfacial waviness, W, in the absence of ageing effects. The rest of the parameter values remain unaltered from Fig. 4 except $h_o = 0.01$

indicate that the increase in the viscosity contrast between the core fluid and the film, brought about by ageing and structure build-up, promotes wave-formation in the nonlinear regime. The associated decrease in wave propagation speed leads to an increase in wave 'density' with decreasing Θ and increasing n for n values that do not result in a transition to 'blow-up'.

3.2.3 Effect of deposition

The flow in the presence of deposition and no ageing is investigated next. In Fig. 10, we show the effect of varying Γ on the quantity $W(t)$, which, in the present case, reflects the increase in the thickness of the layer deposited at the wall starting from a value of $h_o = 0.01$. As can be seen upon inspection of this figure, decreasing Γ gives rise to a sharp increase in $W(t)$. This can be explained by recalling that a decrease in Γ corresponds to an increase in the wall temperature T_w, the partition coefficients, K_1 and K_2, and, ultimately, the flux J.

The increase in the wall layer thickness can be seen clearly in Fig. 11a, which depicts the spatio-temporal evolution of the film for $\Gamma = 1$ with the rest of the parameters remaining the same as in Fig. 10. This figure demonstrates that the film thickness increases sharply near the channel inlet and, at relatively early to intermediate times, appears to remain waveless. At later times, however, perturbations that originate near the inlet are convected downstream and develop into large-amplitude waves, which resemble the ones already discussed above. The core and film temperatures are also shown in Fig. 11b at relatively late times. Here, it can be seen that the core temperature increases from a value of zero at the inlet (which corresponds to the dimensional inlet temperature) with increasing downstream distance due to the heating effect of the wall. The core temperature also exhibits wave-formation in

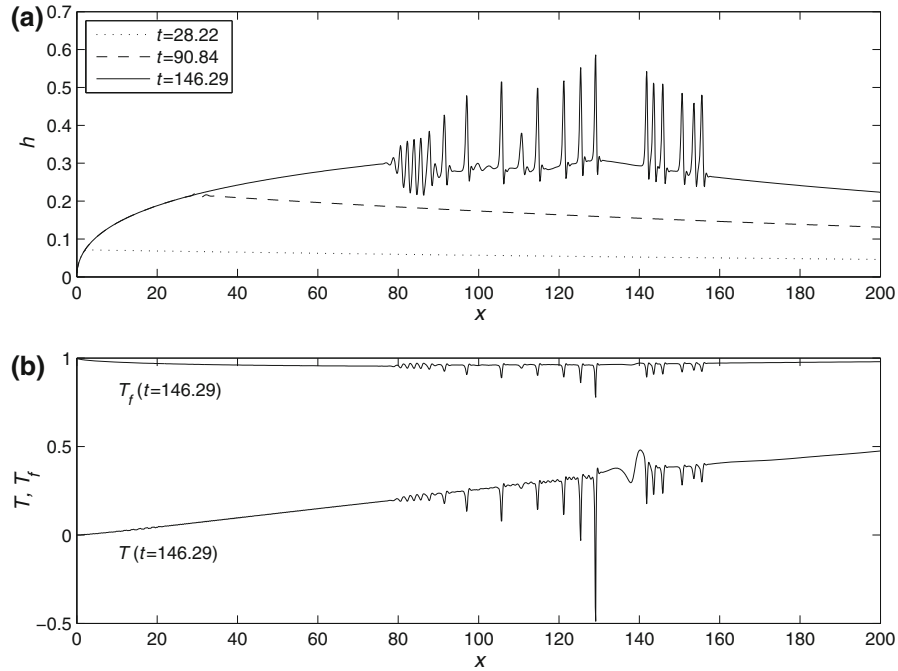

Fig. 11 Interfacial dynamics in the presence of deposition and absence of ageing with $\Gamma = 1$ and the rest of the parameters remaining unaltered from Fig. 10. Panel **a** shows the spatio-temporal evolution of h, while **b** shows T and T_f at $t = 146.29$

response to those developed by the interface, being enslaved to the interfacial dynamics: it is seen that peaks in h correspond to sharp troughs in the core temperature since the resistance to heat transfer from the wall increases with film thickness. The film temperature, T_f, remains close to a value of unity (which corresponds to the dimensional wall temperature) for the duration of the computations, and exhibits very similar wave-formation to that observed in the case of T.

3.2.4 Effect of deposition and ageing

Finally, we study the flow in the presence of ageing as well as deposition. In panels (a) and (b) of Fig. 12, we show similar plots to those already depicted in Fig. 11a and b, which demonstrate the build-up of deposit at the wall and the evolution of interfacial waves. In addition, we show the development of λ_w, which is highest near the channel inlet. Its average value is minimal in the wavy region and then increases gradually with downstream distance. We have also studied the effect of ageing on $W(t)$ for fixed Γ by varying Θ, which characterises the time scale to structure-build. The results shown in Fig. 13 indicate that decreasing Θ, which promotes ageing, leads to a slightly faster increase in $W(t)$.

4 Conclusions

We have studied the dynamics of two-fluid, channel flow in the presence of wall deposition and ageing. The motivating engineering application for this work is crude-oil 'fouling' in pipelines and channels wherein the flow of oil is accompanied by the deposition of wall layers; this results from a phase separation within the oil which consists of a mixture of many components. In such applications, the deposit is known to undergo ageing which is characterised by potentially sharp changes in its rheology. We have derived a coupled system of equations that govern the dynamics

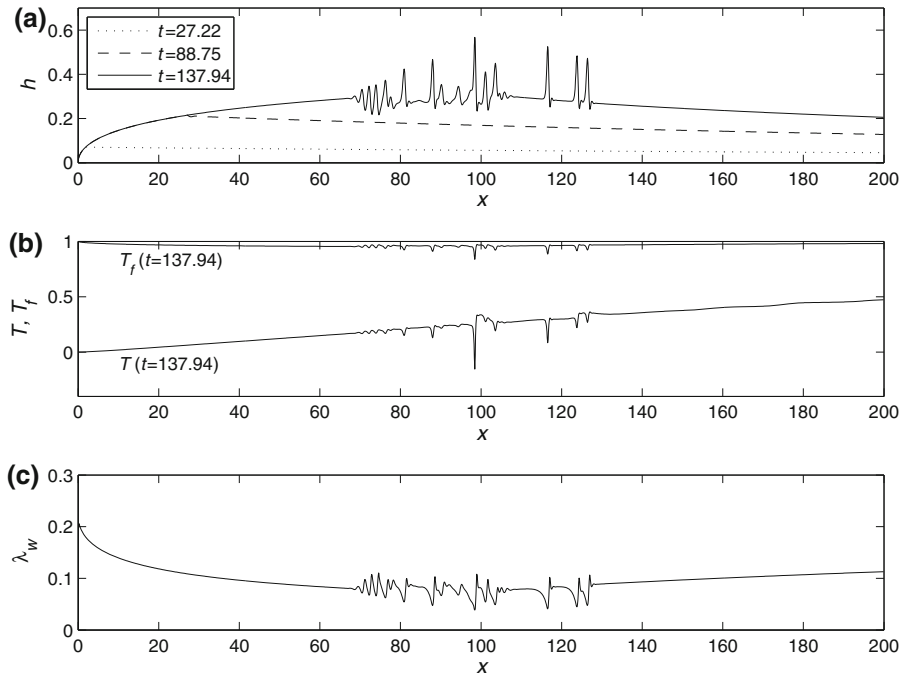

Fig. 12 Interfacial dynamics in the presence of deposition and ageing with $\Gamma = 1$, $n = \alpha = 1$ and $\Theta = 10$; the rest of the parameters remaining unaltered from Fig. 10. Panel **a** shows the spatio-temporal evolution of h, while **b** and **c** show T and T_f, and λ_w at $t = 137.94$, respectively

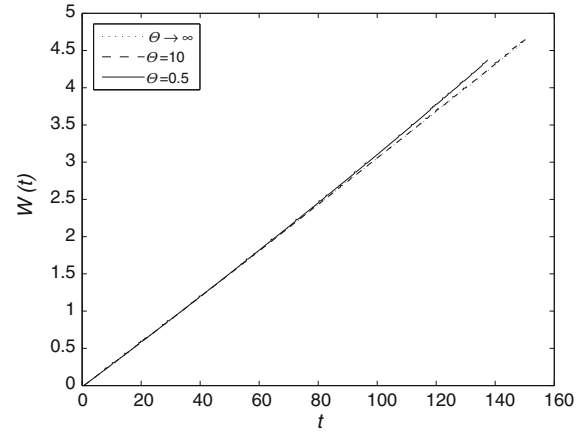

Fig. 13 The effect of varying Θ on the integral measure of the interfacial waviness, W, in the presence of ageing effects. The rest of the parameter values remain unaltered from Fig. 12 except $h_o = 0.01$

of the interface separating the core fluid and the wall deposit, the core and deposit temperature, and the deposit rheology. This is done by employing asymptotic reduction, integral theory and appropriate closure relations for the core temperature and velocity, and deposit rheology.

The deposition is modelled using a Stefan-like flux, which is coupled to the phase-separation process through a chemical-equilibria model used previously to predict wax deposition in oil pipelines [19]. The framework provided by this model allows us to predict the deposition of each of the n components of the oil through a phase transition that depends on the local temperature field which, in turn, is coupled to the flow field. In this paper, $n = 2$ and the oil is considered to be a bi-component mixture. The time-varying deposition rheology is modelled using a Coussot-type relation [14] for a parameter that characterises the internal deposit structure. This is the simplest model that accounts for (potentially rapid) transitions from liquid-like to solid-like behaviour of the deposit.

Our results show that for relatively weak ageing effects, the dynamics are characterised by the formation of solitary wave-trains. Increasing the relative importance of ageing effects results in an increase in the overall waviness of the interface. Deposit ageing is most pronounced in regions where the interface is waveless and the magnitude of the shear is small, leading to significant structure-building within the deposit. Conversely, the latter is diminished in wavy, high-shear regions, such as the ones beneath the crest of a wave.

In certain cases where the transition to solid-like behaviour is so rapid, and/or if the initial structuration level is sufficiently large, the flow characteristics become markedly different: the continuous formation of solitary wave-trains gives way to the development of large-amplitude waves leading to finite-time 'blow-up'. This highlights a deficiency in the model and the necessity to include the relevant physical regularisation to mitigate against the occurrence of 'blow-up'; this may be accomplished via use of 'two-equation' models that couple an evolution equation for the film flow rate to the rest of the model equations [40].

We have also found that increasing the difference in temperature between the wall and the channel inlet promotes phase separation and, therefore wall deposition, leading to rapid thickening of the wall layer. The deposition rate is enhanced slightly via an increase in the relative importance of ageing.

The model discussed in this paper represents one of very few in the literature that provides a theoretical framework for treating the multi-faceted, practically important problem of fouling. This model accounts, for the first time, for the coupling between heat transfer, chemical equilibria, time-varying rheology of the fouling deposit, and the complex interfacial dynamics, characterised by wave formation. Despite the approximations introduced in terms of closures for the velocity, temperature and viscosity fields, this model provides a tool for the prediction of fouling rates in practical, engineering settings. It is extensible in a straightforward manner to multi-component, multi-phase mixtures, and can easily accommodate more faithful representations of the deposit rheology, and more accurate closures for the velocity and temperature fields.

Acknowledgement The authors acknowledge the support of the Engineering and Physical Sciences Research Council, UK, through grant number EP/D503051/1.

Appendix: Chemical equilibria

Here, we outline the derivation of the expression for the deposition flux, which gives rise to and then thickens the wall layer, referred to in the main text as the 'film' or 'deposit' [19]. We consider the core fluid to be composed of a two-phase, mixture of n components, and specialise at the end of the derivation to the $n = 2$ case. For each component, i, one has

$$x_i L_x + d_i L_d = z_i L_{\text{tot}}, \tag{78}$$

where $L_x + L_d = L_{\text{tot}}$ in which L_x and L_d denote the number of moles in the liquid and precipitated 'solid' phase, respectively, and L_{tot}, is the total number of moles in the mixture; here, we shall work with a basis of one mole; x_i and d_i represent the mole fractions of component i in the liquid and 'solid' phases, respectively, while z_i is the total mole fraction of component i. The fractions x_i and d_i are related by the following partition coefficients

$$K_i = \frac{d_i}{x_i} = K_{i0} \exp\left[-\frac{\triangle H_{pi}}{RT}\left(1 - \frac{T}{T_{pi}}\right)\right], \quad i = 1, 2 \ldots, n, \tag{79}$$

in which ΔH_{pi} and T_{pi} denote the precipitation enthalpy and temperature of component i, respectively, and K_{i0} is the value of the equilibrium coefficient when $T = T_{pi}$. The mole fractions x_i, d_i and z_i also satisfy the following relations:

$$\sum_{i=1}^{n} x_i = \sum_{i=1}^{n} d_i = \sum_{i=1}^{n} z_i = 1. \tag{80}$$

The weight fraction of each component of the mixture, χ_i, is defined by:

$$\chi_i = \frac{z_i M_i}{\sum_p^n z_p M_p}, \tag{81}$$

where M_i is the molecular mass of component i. The weight fraction of each component i present in the precipitated phase is

$$\chi_{di} = \frac{L_d d_i M_i}{\sum_p^n z_p M_p} = \chi_i \frac{L_d d_i M_i}{z_i M_i}, \tag{82}$$

which we re-express as

$$\chi_{di} = \chi_i \frac{\theta K_i}{1 + \theta K_i}, \tag{83}$$

where θ is given by

$$\theta \equiv \frac{L_d}{L_x} = \frac{1 - L_x}{L_x}. \tag{84}$$

The total weight fraction of the precipitated phase is expressed by

$$\chi_d = \sum_{i=1}^{n} \chi_{di} = \sum_{i=1}^{n} \chi_i \frac{\theta K_i}{1 + \theta K_i}. \tag{85}$$

In order to develop an equation for J, we start from Fick's law of diffusion for the precipitated phase which diffuses to the wall region:

$$J = D_s \rho_{d,n}, \tag{86}$$

where the total, constant, density is taken to be the sum of the densities of the precipitated and fluid phases: $\rho = \rho_d + \rho_x$; then, one may write, $\rho_d = \rho \chi_d$ and $\rho_x = \rho(1 - \chi_d)$ so that the flux, J, can be re-expressed in terms of $\chi_d : J = D_s \rho \chi_{d,n}$.

In order to relate J to temperature variations in the core fluid, one writes

$$J = D_s \rho \chi_{d,T} T_n = D_s \rho \frac{\eta}{T} T_n, \tag{87}$$

where

$$\eta = \sum_{i=1}^{n} \eta_i,$$

in which η_i are given by

$$\eta_i = T \chi_{di,T} = \chi_i \frac{\left[T(1+\theta)^2 \frac{\partial L_x}{\partial T} + \theta \frac{\triangle H_{pi}}{RT} \right] K_i}{(1 + \theta K_i)^2}, \tag{88}$$

where use has been made of (83) and (84).

We now consider the specific case of a bi-component mixture, so that $n = 2$. For this case, the quantity L_x becomes $L_x = b/a$ where a and b, which are functions of the partition coefficients $K_1(T)$ and $K_2(T)$, and are given by

$$a = 1 + K_1 K_2 - K_1 - K_2, \tag{89}$$

$$b = K_1 K_2 - z_1 K_2 - z_2 K_1; \tag{90}$$

then the variation of the number of moles in the fluid phase with respect to core fluid temperature is given:

$$L_{x,T} = \sum \left\{ [(b - a) K_i + (a z_i - b)] \triangle H_{p(3-i)} K_{(3-i)} \right\} R T^2 a^2. \tag{91}$$

In order to obtain a dimensionless expression for flux, to leading order in the parameter ϵ, we substitute the scaling given by Eqs. (22) in (79), (87), (88) and (91) to finally get (after suppression of the bar decoration)

$$J = \frac{1}{\mathrm{Pe}} \left[\frac{\eta}{(T + \Gamma)} \frac{\left(T_z - \epsilon^2 h_x T_x \right)}{\left(1 + \epsilon^2 h_x^2 \right)^{1/2}} \right]_{z=h} = \frac{1}{\mathrm{Pe}} \left[\frac{\eta}{(T + \Gamma)} T_z \right]_{z=h} + O(\epsilon^2), \tag{92}$$

in which $\eta = \eta_1 + \eta_2$ where η_i $(i = 1, 2)$ are given by

$$\eta_i = \frac{\chi_i K_i}{(1 + \theta K_i)^2} \left[\Delta T \, (T + \Gamma) \, (1 + \theta)^2 \, L_{x,T} + \theta \beta_i \frac{1}{(T + \Gamma)} \right], \tag{93}$$

where the dimensionless $L_{x,T}$ and K_i $(i = 1, 2)$ are, respectively, expressed by

$$L_{x,T} = \frac{1}{\Delta T} \sum \left\{ [(b - a) \, K_i + (a z_i - b)] \, \beta_{(3-i)} K_{(3-i)} \right\} (T + \Gamma)^2, \tag{94}$$

$$\frac{K_i}{K_{i0}} = \exp \left[- \frac{\beta_i}{(T + \Gamma)} \left(1 - \frac{\Omega_i \, (T + \Gamma)}{\Gamma} \right) \right], \quad i = 1, 2. \tag{95}$$

Here, $\Gamma \equiv \frac{T_{in}}{\Delta T}$, $\beta_i \equiv \frac{\Delta H_{Pi}}{\Delta T R}$, and $\Omega_i \equiv \frac{T_{in}}{T_{pi}}$.

References

1. Weinstein SJ, Ruschak KJ (2004) Coating flows. Annu Rev Fluid Mech 36:29–53
2. Stone HA, Strook AD, Ajdari A (2004) Engineering flows in small devices. Annu Rev Fluid Mech 36:381–411
3. Squires TM, Quake SR (2005) Micro-fluidics: fluid physics at the nanoliter scale. Rev Mod Phys 77:977–1024
4. Grotberg JB (1994) Pulmonary flow and transport phenomena. Annu Rev Fluid Mech 26:529–571
5. Grotberg JB (2001) Respiratory fluid mechanics and transport processes. Annu Rev Biomed Eng 3:421–457
6. Shyy W, Francois M, Udaykumar HS, N'dri N, Tran-Son-Tay R (2001) Moving boundaries in micro-scale biofluid dynamics. Appl Mech Rev 54:405–453
7. Gallez D, Coakley WT (1996) Far-from-equilibrium phenomena in bioadhesion processes. Heterog Chem Rev 3:443–475
8. Oron A, Davis SH, Bankoff SG (1997) Long-scale evolution of thin liquid films. Rev Mod Phys 69:931
9. Myers TG (1998) Thin films with high surface tension. SIAM Rev 40:441–462
10. Craster RV, Matar OK (2009) Dynamics and stability of thin liquid films. Rev Mod Phys 81:1131–1198
11. Ramirez-Jaramillo E, Lira-Galeana C, Manero O (2006) Modelling asphaltene deposition in production pipelines. Energy Fuels 20:1184–1196
12. Boek ES, Ladva HK, Crawshaw JP, Padding JT (2008) Deposition of colloidal asphaltene in capillary flow: experiments and mesoscopic simulation. Energy Fuels 22:805–813
13. Liu AJ, Nagel SR (1998) Jamming is not just cool any more. Nature 396:21
14. Coussot P, Roussel N, Jarny S, Chanson H (2005) Continuous or catastrophic solid–liquid transition in jammed systems. Phys Fluids 17:011704
15. Roussel N, Roy RL, Coussot P (2004) Thixotropy modelling at local and macroscopic scales. J Non-Newton Fluid Mech 117:85
16. Huynh HT, Roussel N, Coussot P (2005) Aging and free surface flow of a thixotropic fluid. Phys Fluids 17:033101
17. Coussot P, Nguyen QD, Huynh HT, Bonn D (2002) Avalanche behaviour in yield stress fluids. Phys Rev Lett 88:175501
18. Coussot P, Nguyen QD, Huynh HT, Bonn D (2002) Viscosity bifurcation in thixotropic, yielding fluids. J Rheol 46:573
19. Svendesn JA (1993) Mathematical modelling of wax deposition in oil pipeline systems. AIChE J 39:1377–1388
20. Shkadov VY (1967) Wave flow regimes of a thin layer of viscous fluid subject to gravity. Fluid Dyn Res 2:21–34
21. Ruyer-Quil C, Manneville P (1998) Modelling film flows down inclined planes. Eur Phys J B 6:277–292
22. Matar OK, Lawrence CJ, Sisoev GM (2005) The flow of a thin film over a spinning disc: hydrodynamics and mass transfer. Phys Fluids 17:052102
23. Ruyer-Quil C, Scheid B, Kalliadasis S, Velarde MG, Zeytounian RK (2005) Thermocapillary long waves in a liquid film flow. Part 1. Low-dimensional formulation. J Fluid Mech 538:199–222
24. Scheid B, Ruyer-Quil C, Kalliadasis S, Velarde MG, Zeytounian RK (2005) Thermocapillary long waves in a liquid film flow. Part 2. Linear stability and nonlinear waves. J Fluid Mech 2538:223–244
25. Matar OK, Lawrence CJ, Sisoev GM (2007) Interfacial dynamics in pressure-driven two-layer laminar channel flow with high viscosity ratios. Phys Rev E 75:056314
26. Trevelyan PMJ, Kalliadasis S (2004) Dynamics of a reactive falling film at large Peclet numbers. II. Nonlinear waves far from criticality: integral-boundary-layer approximation. Phys Fluids 16:3209–3226
27. Trevelyan PMJ, Scheid B, Ruyer-Quil C, Kalliadasis S (2007) Heated falling films. J Fluid Mech 592:295–334
28. Kapitza PL (1948) Wave flow of a thin viscous fluid layer. I. Free flow. J Exp Theor Phys 18:3–20
29. Scheid B, Ruyer-Quil C, Manneville P (2006) Wave patterns in film flows: modelling and three-dimensional waves. J Fluid Mech 562:183–222
30. Delhaye JM (1974) Jump conditions and entropy sources in two-phase systems. Local instant formulation. Int J Multiph Flow 1:395–409
31. Burelbach JP, Bankoff SG, Davis SH (1988) Nonlinear stability of evaporating/condensing liquid films. J Fluid Mech 195:463
32. Zadražil A, Stepanek F, Matar OK (2006) Droplet spreading, imbibition and solidification on porous media. J Fluid Mech 562:1–33

33. Sileri D, Ding H, Matar OK (2010) Direct numerical simulations of channel flows with phase separation and ageing effects (in preparation)
34. Keast P, Muir PH (1991) Algorithm 688 EPDCOL—a more efficient PDECOL code. ACM Trans Math Softw 17:153–166
35. Zhang YL, Craster RV, Matar OK (2003) Analysis of tear film rupture: effect of non-Newtonian rheology. J Colloid Interface Sci 262:130–148
36. Kumar S, Matar OK (2004) Dewetting of thin liquid films near soft elastomeric layers. J Colloid Interface Sci 273:581–588
37. Balmforth NJ, Bush JWM, Craster RV (2005) Roll waves on flowing cornstarch suspensions. Phys Lett A 338:479–484
38. Duprat C, Giorgiutti-Dauphine F, Tseluiko D, Saprykin S, Kalliadasis S (2009) Liquid film coating a fiber as a model system for the formation of bound states in active dispersive-dissipative nonlinear media. Phys Rev Lett 103:234501
39. Benney DJ (1966) Long waves on liquid films. J Math Phys 45:150–155
40. Ruyer-Quil C, Manneville P (2000) Improved modelling of flows down inclined planes. Eur Phys J B 15:357–369